Journal of Materials Chemistry A

Accepted Manuscript

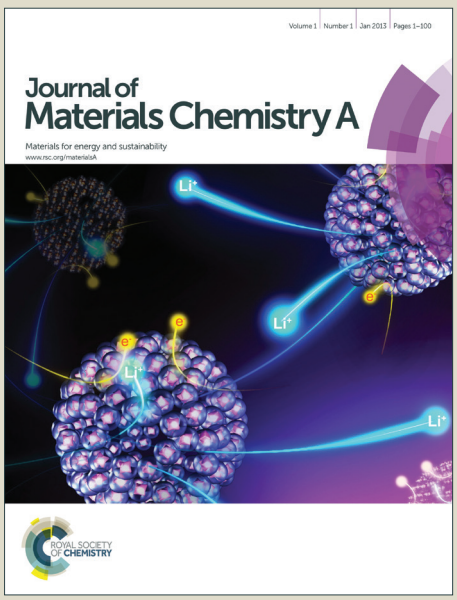

ROYAL SOCIETY OF CHEMISTRY

www.rsc.org/materialsA

Journal Name

RSCPublishing

COMMUNICATION

Integration of Sn/C Yolk-Shell Nanostructures into Free-standing Conductive Networks as Hierarchical Composite 3D Electrodes and the Li-ion Insertion/ Extraction Properties in a Gel-type Lithium-ion Battery Thereof

Cite this: DOI: 10.1039/xoxxooooox

Received ooth January 2012,
Accepted ooth January 2012

DOI: 10.1039/xoxxooooox

www.rsc.org/

Wei Ni,[ac] Jianli Cheng,[ac] Lingying Shi,[b] Xiaodong Li,[ac] Bin Wang,*[ac] Qun Guan,[ac] Ling Huang,[ac] Guifang Gu[ac] and Hang Li[b]

A novel style of Sn/C yolk-shell nanospheres integrated into nanofibrous 3D electric conducting structures as free-standing materials for potential applications such as new-generation anode structures for gel-type lithium-ion batteries *via* the design principle of inhibiting the aggregation of tin nanoparticles, buffering the occurring volume strain, and the flexible conductive networks.

Introduction

New materials, particularly nanostructured materials have attracted tremendous interests in recent years, due to their unusual properties for a potential new generation of energy devices as well as the environmental concerns.[1-8] Hierarchical three-dimensional (3D) electric conducting networks in nano- and micro-scale, such as the nanocable-like structure,[9, 10] graphene-based networks[11, 12] have offered great advantages and became an ideal candidate for the structural backbone and current collector.[13, 14-16] The application of 3D electrode structures have made the future of lithium-ion batteries quite bright in view of the higher specific capacity, much improved rate performance, as well as superior cycling stability brought by the powerful nanotechnology tool in the design of new electrode materials for lithium-ion batteries, especially for high-capacity electrode materials with large volume variations and low electrical conductivities.

For lithium-ion batteries, as a main power source for portable electronic devices and the promising fields of electric grids, electric vehicles, a great deal of attempt has been made to develop new electrode materials with exquisitely designed structures to meet the demand for batteries of higher energy density and improved cycle performances.[17] Among the anode materials, silicon (Si), germanium (Ge), and tin (Sn) *etc.* elementary substances provide promising alternative to conventional carbonaceous ones, due to their much higher capacity density *via* alloying reversibly with more lithium, such as tin has a theoretical specific capacity of 992 mAh g^{-1} ($Li_{4.4}Sn$) over that of conventional graphite of 372 mAh g^{-1} (LiC_6),[18] as well as the eliminated irreversible charge losses caused by solvent intercalation. At the meantime, to overcome the huge challenges suffered from large volume variation during lithium-ion insertion/extraction cycles (*ca.* 260% based on the densities of bulk Sn and fully lithiated tin) which will lead to very rapid capacity decay due to serve pulverization or agglomeration in the anode electrode,[19] many kinds of appropriate structure design based on tin materials have been exploited for relatively higher specific capacity as well as better cycle performances. As we know that yolk/shell or 'rattle-typed' nanomaterials with nanoparticle cores inside hollow shells are of special interest among the complex hollow nanostructures, which are promising functional candidates for a variety of applications such as selective catalysis, controlled delivery, advanced lithium-ion batteries and biosensors due to the tailorability and functionality in both cores and hollow shells.[17, 20-26] Based on this principle, some pioneering researches such as tin-encapsulated spherical hollow carbon structures by pyrolysis of tin-containing organic precursors or by a colloid template assisted pyrolysis process have been designed for better electrochemical performances.[22, 17] The carbon shell for the above yolk-shell or rattle-type structures has itself good electric conductivity and prevents the aggregation of active materials *via* excellent elasticity to effectively accommodate the strain of volume change during Li^+ insertion/extraction just like some other hollow transition metal oxides/carbon nanocomposites reported with high capacity and capacity retention as anode materials.[27, 28] However, one of the main drawbacks that need to be pointed out is that the classical or traditional yolk-shell structures are typically of particulate morphology and are usually cohered by additives such as polymer binders and conductive carbon. The gaps between the particles may eventually deteriorate the structural integration and may suffer more challenges in application of next-generation flexible or wearable electric devices. The fabrication of complex hollow nanostructures into 3D electrodes would be of great interest and may show potentials in optimized Li-ion anodes. Since the optimized design principle has been primarily introduced into the fabrication of electrochemical capacitors, for instance, cobalt oxide hollow nanoparticles incorporated in flexible carbon nanofiber film as self-supported electrodes have been explored for supercapacitors.[29]

Here we further design the strategy to integrate the Sn/C yolk-shell structures and the concept of 'hierarchical 3D electric conducting networks' to fabricated a novel free-standing 3D nanostructure as lithium-ion anodes, which gets rid of the use of

polymer binders, conducting carbon black and copper current collectors, to meet the aim of more cost-effective and environmentally friendly batteries of the future.

Results and discussion

As described in **Scheme 1**, it shows the *in situ* formation of Sn nanoparticle/buffering carbon shell (Sn@C yolk-shell) nanospheres integrated in carbon nanofibers by one-step pyrolysis–reduction process of electrospun SnO_2 hollow sphere/polyacrylonitrile (PAN) core-shell fibers. The process is depicted briefly as follows, the well dispersed composite slurry was firstly electrospun to generate the SnO_2 hollow sphere/PAN sub-microfibers, which were then pyrolyzed at 800 ^oC under hydrogen atmosphere to obtain the Sn/C yolk-shell structures embedded in carbon nanofiber backbones via an *in situ* reduction process (experimental details see Experimental Section).

Pristine SnO_2 hollow spheres (SnO_2HSs) were first prepared by a facile one-pot hydrothermal method according to literature recipes shown in the Experimental Section. As shown in our previous study, relatively uniform SnO_2 nanospheres with diameters of ~200 nm, shell thickness of ~30 nm were obtained.[30] By electrospinning the as-prepared SnO_2 hollow spheres into a polymer substrate (e.g. PAN), the necklace-like 'SnO_2HSs stringed by PAN nanofibers' structure was fabricated. The scanning electron microscopy (SEM) images in **Figure 1** reveal the morphology of the as-prepared hierarchical SnO_2HSs@PAN fibers, which displays a uniform diameter distribution of *ca.* 600 nm for the PAN backbone, and main size distribution of *ca.* 450–550 nm for the SnO_2HSs@PAN core-shell microsphere subsystem structure.

The as-collected SnO_2@PAN free-standing paper-like composites were first stabilized in air (pre-oxidation) at 200 ^oC for 10 h, beneficial for a well preserved morphology after carbonization. The carbonization was conducted under a hydrogen atmosphere, and the composite fibers were finally transformed into Sn@C yolk-shell nanospheres integrated in carbon nanofibers, with carbon backbone average diameter of ~400 nm, carbon-shell size in the range of 430–820 nm with embedded nanopores of mainly 1–2 nm, and the tin yolks show a typical diameter of *ca.* 270–470 nm, as representatively shown in **Figure 2**. As shown above, the SnO_2@PAN can alternatively be transformed to a Sn@C yolk-shell subsystem structure by an *in situ* self-sacrificing reduction process in a nitrogen atmosphere, which could be regarded as a reverse process of Sn@C oxidation, as reported that Sn@C structures may reversely transform to SnO_2@C hybrid hollow spheres by a self-templating methodology *via* the nanoscale Kirkendall effect.[31] Compared with some reported works on Sn nanoparticles inside/at the surface of electrospun fibers, where the precursors of the Sn component are mostly restricted to tin salts,[32-37] the yolk-shell integrated 3D nanofibrous structure may be endowed with better tailored buffering space as well as electric conductivity.

The XRD analysis confirmed the composition and crystal structures of the above-mentioned SnO_2@PAN and Sn@C free-standing nanofibrous composite materials. As revealed in **Figure 3a**, the XRD diffraction peaks shown in 'SnO_2@PAN' sample can be assigned undisputedly to tetragonal rutile SnO_2 phase (cassiterite, JCPDS file no. 41-1445; space group: $P4_2/mnm$, a_o = 4.738 Å, c_o = 3.187 Å).[38-42] The sharp XRD peaks of the 'Sn@C' sample can be well indexed to the tetragonal metallic Sn phase (JCPDS file no. 86-2265) of high crystallinity and no SnO_2 residue was found.[17, 43] Furthermore, an additional weak and broad peak appeared at 2θ of about 24.5–27.5^o in Sn@C sample comes from the carbon backbones.[44, 45]

The graphitic structure of the carbon shells of the Sn@C composite could be further revealed from the Raman spectroscopy (**Figure 3b**). Two characteristic peaks of *ca.* 1340 and 1600 cm^{-1} can be attributed to D band arising from the defects and disorders in carbonaceous solid and G band from the stretching mode of C–C bonds of typical graphite, respectively.[46, 47] The intensity ratio of (I_D/I_G) of the two bands is about 0.91 (G-band peak intensity higher than that of D-band), further indicating the relatively low graphitization degree of the as-obtained carbon shell structures over the tin cores. The discontinuous carbonaceous layers and numerous defects in the shells of the composite structures may be propitious to the diffusion of Li-ions. The specific surface area, mainly contributed by the carbon shell, calculated with the Brunauer–Emmett–Teller (BET) model by the nitrogen adsorption/desorption isotherms of the Sn/C composite is 151 $m^2\ g^{-1}$. The average pore size calculated from the desorption data is 5.4 nm, and the total pore volume is 1.04 $cm^3\ g^{-1}$ by the Barrett—Joyner–Halenda (BJH) method from the desorption branch of nitrogen isotherm (**Figure S3** in ESI†). The nitrogen sorption analysis and the higher resolution SEM images of the Sn@C nanocomposite showed that the carbon shell frameworks possessed a bimodal nanoporous structure; the presence of large pores will enable the buffering of volume strain and the suppression of aggregation of Sn component, while small pores will benefit rapid electrolyte transport. These small pores are primarily responsible for the surface area determined for the composite. On the other hand, thermogravimetric analysis (TGA) results of the Sn/C structures under air atmosphere were recorded to determine the mass composition of Sn/C structures derived from varied chemical reduction conditions including temperature and time (as shown in **Figure S4** in ESI†). The mass of the samples basically kept stable below 200 ^oC, and with the increase of temperature, the following reactions occurred:

$$C + O_2 \rightarrow CO_2\ (gas)$$
$$Sn + O_2 \rightarrow SnO \rightarrow SnO_2$$

The chemical oxidation of C to CO_2 resulted in a mass decrease while the oxidation of Sn to SnO and SnO_2 a mass increase, so the TGA curves exhibited a first mass increase then decrease trend related with these actions. After the temperature rose to 800 ^oC, the total oxidation reactions completed and all carbon and tin in the Sn@C composite structures had converted to CO_2 and SnO_2, respectively.[17] It can be accordingly determined that the Sn@C composite has a chemical composition of *ca.* 44 wt.% tin and 56 wt.% carbon for the sample in Figure 2. And the Sn content may be regulated by the control of pyrolysis conditions for a wide range from 44 to 78 wt.%, for example.

Taking into consideration of the safety factors, we herein adopted the semi-solid electrolytes. Since the unconventional electrolytes, including solid electrolytes (ceramic, polymeric and composite), polymer electrolytes, such as poly(vinylidene fluoride) (PVDF)-based fibrous polymer electrolytes, microporous PVdF gel, play an important role for lithium-ion batteries. For example, PVDF has a good electrochemical and temperature stability and it plays an advantageous role as polymer-based electrolytes.[48-52] The following test data of electrochemical performances are based on cells equipped with a PVDF microporous separator (see **Figure S5** in ESI †). The cyclic voltammetry (CV) profile of the Sn/C yolk-shell free-standing electrode within a potential window of 3–0 V *vs.* Li/Li^+ at a scan rate of 0.05 mV s^{-1} is shown in **Figure 4a**. There is a pronounced decrease of cathodic current between the first and the second CV for the Sn/C–Li half cell. The similar phenomena were reported in previous Sn-based anode materials and can be attributed to the irreversible reaction and the formation of solid electrolyte interface (SEI) layer.[53] Furthermore, it can be seen that three major smooth anodic peaks exist in the stabilized CV curve, which match with that given in other reports (see Note S1 in ESI† for illustration in detail),[54-56] and are corresponding to the Li^+ extraction profiles

and to the Galvanostatic plateaus in **Figure 4b** (Galvanostatic half-cell cycling see **Figure S6** in ESI†). The novel Sn@C nanocomposite shows an initial capacity of 979 mAh g^{-1}, for Li storage in the potential window of 2–0.01 V at 50 mA g^{-1} (i.e. ~100 mA cm^{-2}). The electric potential during the alloying and dealloying of lithium from the Sn@C composite negative electrode material varied as the phases of Li-Sn present in the electrode change, where the Sn component was subjected to the subsequent conversion reactions ($Li_xSn \leftrightarrow Sn^0$). This potential profile matches well with that of a tin negative electrode calculated and measured by Courtney *et al.* for the lithiation of tin.[57] And the large irreversible capacity for the oxygen containing materials, e.g. SnO_x, is partly eliminated. **Figure S7** in ESI† shows the Nyquist plots *via* electrochemical impedance spectroscopy (EIS). In the middle-to-low frequency region, a 45° line, can be associated to diffusion in presence of a block electrode. And at intermediate frequencies, it is deduced that the diffusion takes place through porous and heterogeneous carbon shell. A high-frequency feature, is commonly describing Li^+ migration through a conductive passivation. The charge-transfer resistance (T_{ct}), which is believed to be one of the important factors in electrochemical reactions, is reflected in the diameter of the semicircle along the Z′ axis. The T_{ct} of the activated Sn@C yolk-shell free-standing anode (after 5 cycles) is estimated to be reduced by 76 % as contrasted to that of the pristine Sn@C anode. The decreasing of resistance may be attributed to a catalytic action of the encapsulated Sn nanoparticles toward the Li^+ desolvation step at carbon/electrolyte interface, thus enhancing lithium insertion rate and reducing the polarization related to charge-transfer process.[33, 58, 59]

The Sn/C composite as a single electrode in a half cell is usually not sufficiently to claim its practical relevance as a novel anode material in a lithium-ion battery. Herein a full cell where the Sn@C yolk-shell free-standing composite electrode (binder-free anode) was coupled with a most commercialized $LiCoO_2$ cathode in a 1 M $LiPF_6$ EC/DMC gel-type electrolyte (PVDF microporous seperator). For the $LiCoO_2$-acetylene black cathode, it delivered a stable potential of ~3.8 V and capacity of ~130 mAh g^{-1} with a cut-off voltage range of 4.2–2 V and current density of 50 mA g^{-1} (**Figure S8** in ESI†) , though the acetylene black powder may agglomerate and is separated from $LiCoO_2$ particles by the binder PTFE.[60] Although it could reach up to a capacity of ~150 mAh g^{-1} with a wider cut-off voltage range of 4.5–2 V, the capacity dropped sharply mainly due to a fatal structural failure.[61]

The performances of the full battery cells in terms of capacity (referred to the anode) versus potential cut-off window and/or cycle number are illustrated in **Figure 4c&d**. The theoretical specific capacity of tin and carbon is 992 mAh g^{-1} and 372 mAh g^{-1}, respectively, so the Sn@C (with Sn mass fraction of *ca.* 44%) has a theoretically calculated specific capacity of 645 mAh g^{-1}. The electrochemical characteristics of the Sn/C composite are maintained in the full cell, it delivered an initial charge and discharge capacity of 893 and 599 mAh g^{-1} in the potential cut-off window of 4.0–1.5 V with a mid-value discharge potential of 3.15 V and Coulombic efficiency (CE) of 67%, and the CE increased from 81% to 95 % during the following few cycles, and cycled with a specific capacity higher than 440 mAh g^{-1} in the initial 10 cycles. The Sn/C composite electrode suffered from an irreversible capacity loss in the first cycle which largely results from the electrolyte decomposition on carbon surface.[22] By subtracting the capacity of carbon shell (372 mAh g^{-1}), the discharge specific capacity in a full cell by the Sn component (44 wt.%) was estimated to be 889 mAh g^{-1}, which amounts to about 90% of the theoretical value (992 mAh g^{-1}). With a widened potential cut-off window, e.g. 4.2–1.2 V, the capacity of the full cell shows an increase of *ca.* 29%, i.e. from 440 to 567 mAh g^{-1}. The increase in discharge capacity can be ascribed to the further enhanced delithiation effect for the Sn/C anode in the Li^+ insertion/extraction process. However, a further higher charge potential (e.g. 4.5 V) would lead to the destruction of $LiCoO_2$ cathode and the capacity of the full cell dropped drastically in the following cycles after an eruption. Nevertheless, the Coulombic efficiency may be further improved by a pre-lithiation process of the Sn@C anode for better long-term performance upon electrochemical charge/discharge cycling.[62]

In addition, it may be stressed that when the Sn/C composites were derived by the pyrolysis of SnO_2@PAN under a nitrogen atmosphere instead of hydrogen atmosphere, the carbon shells might offer a self-sacrificing reduction effect for the SnO_2 cores, and would usually render the Sn/C composite with a higher Sn content. The difference is that there were four separate peaks at 0.5–0.8 V for the anodic scanning loop, which are related to the dealloying reaction of Sn component (i.e., Li^+ extraction from Li_xSn alloys),[22] and these phenomena are also revealed in Sn@graphene structures with exposed tin nanoparticles.[53, 63] **Figure S9–S11** in ESI† shows the features of the Sn/C hierarchical nanocomposites with partly exposed tin nanoparticles and the differential current density versus potential curves, where the sharp peaks appearing in the Sn/C–Li cell well match those in a Sn–Li cell. For most Li/tin-oxides anode materials, sharp features may not be noted due to the absence of the formation of two phase regions.[64, 65] The relative sharp peaks were alternatively appeared as charge or discharge plateaus in tiers for a galvanostatic mode, which would also be revealed in the full cell of $LiCoO_2$–Sn/C system. The phenomena might be basically ascribed to the unrestricted Li^+ insertion/extraction processes. Furthermore, the freestanding Sn/C composite with exposed tin microspheres derived from higher SnO_2 content in the electrospinning slurry (i.e., 75 wt.% in SnO_2/PAN precursor) showed the similar electrochemical characteristics and the specific capacity faded faster as well (**Figure S12** in ESI†), the analogous phenomena were reported elsewhere in literature.[66]

Conclusions

In summary, a novel approach was designed to prepare a kind of 3D electrodes of integrated Sn/C yolk-shell composite structures. The tin nanoparticles encapsulated in the elastic hollow carbon spheres which were integrated in a porous electron-conductive network, may have great potentials for the next-generation flexible or wearable electronic devices. Not only is this approach a further example of the directed nanostructure design of free-standing networks with elastic hollow carbon spheres as buffer and container for lithium-ion batteries, but also the strategy could be extended to other anode and cathode materials or as novel substrates for applications in nanoreactors, controlled release and selective adsorption fields.

Experimental section

Materials: A polyacrylonitrile (PAN, average M_W 150,000 (Typical); Aldrich) solution with a concentration of *ca.* 10–14 wt.%, prepared by dissolving SnO_2 hollow spheres and PAN powder (with mass ratio of 0.200 g / 0.264 g, or 0.737 g / 0.243 g) in *N,N*-dimethylformamide (DMF, 1.94 g or 2.42 g) at room temperature with vigorous stirring overnight, was used for electrospinning process. The $LiCoO_2$ particles (99.8% metals basis, Aladdin Reagent, China) were used directly without post-treatment as cathode materials for a $LiCoO_2$–Sn/C full cell.

Samples Preparation: SnO_2 hollow spheres were synthesized via a classic one-pot, template-free, hydrothermal route by Prof. Lou *et al.* in the literature.[41] Typically, a fixed amount of potassium stannate

trihydrate (0.384 g, $K_2SnO_3 \cdot 3H_2O$, 99.5% metal basis; Aladdin) and urea (0.48 g, ≥ 99.0%; Chengdu Kelong Chemical Reagent Co., China) was dissolved in a mixture solution of deionized water (50 mL) and ethanol (30 mL, ≥ 99.7%) under continuous stirring. The clear solution was then swiftly transferred into a Teflon-lined stainless steel autoclave (with a volume of *ca.* 100 mL), followed by heating at 200 ºC for 24 h in an electric oven. Afterwards, the autoclave was cooled naturally to room temperature. The white precipitate was collected by centrifugation, washed with ethanol for several times, and then dried at 60 °C overnight. For the preparation of classical cathode electrode, a slurry mixture of $LiCoO_2$ power, acetylene black (AB), and poly(vinylidene fluoride) (PVDF) with a weight ratio of 8:1:1 was spread on a piece of Al foil, and dried at 80 °C in vacuum overnight.

A piece of grounded aluminum foil was placed 20 cm below the single-nozzle spinneret to collect the nanofibers. A high voltage of 20 kV was supplied at the spinneret by a direct-current power supply, and the typical feeding rate was set at *ca.* 30 μL min^{-1}. All the samples were collected at room temperature in air atmosphere. The collected electropun paper of SnO_2HSs/PAN nanofibers was tailored and transferred to a tube furnace and calcined typically at 800 °C in hydrogen or nitrogen atmosphere for 5 min or 0.5 h with a heating rate of 20 °C min^{-1} to obtain Sn/C yolk-shell composite nanofiber paper.

Characterization*:* The composition and crystal structures of the samples were obtained by X-ray diffraction analysis (XRD, PANalytical X'Pert Pro, Cu Kα radiation, λ = 1.5418 Å) over a 2θ range of 10 to 90°. The surface morphology was investigated using scanning electron microscopes (FE-SEM, ZEISS Ultra 55; TESCAN VEGA3) operating at 15–20 kV after Pt coating. Transmission electron microscopy (TEM) was performed using a JEOL JEM-100CX operating at 80 kV. Thermogravimetric analysis (TGA) was conducted on a TGA 1, STAR^e System (Mettler Toledo) to determine the thermal decomposition process and the weight ratio of Sn in the composite at a heating rate of 20 °C min^{-1} between 50 and 1000 °C. Raman spectra were collected on a Jobin-Yvon LabRam HR80 spectrometer with excitation from Torus 50 mW diode-pumped solid-state laser (532 nm). Nitrogen adsorption and desorption isotherms were carried out at 77 K on a surface area and pore size analyzer (BK300, Beijing JWGB Sci&Tech Co., Ltd.) after degassing at 200 °C for 3 h under vacuum in the degas port.

Electrochemcial characterization*:* The obtained Sn/C nanofibrous paper was cut into squares of *ca.* 1×1 cm^2 weighted ~2.0 mg, and used as free-standing electrodes with lithium plate as the counter electrode and reference electrode, with 1 M $LiPF_6$ in EC/DMC (v/v = 1:1) as electrolyte, with porous PVDF (pore size 0.45 μm) as a gel-type polymer separator membrane. For the full Li-ion battery, the classic $LiCoO_2$-AB (acetylene black) cathode was used as the cathode and the as-preapred Sn@C 3D nanostructrures as a free-standing anode.

The CR2032 coin cells were assembled in an argon-filled glovebox (Vigor, with SOTA Standard), where moisture and oxygen levels were kept below 1 ppm. Electrochemcial experiments were carried out on the LANHE CT2001A battery testing system (Wuhan Land Electronic Co., China) for cycling characteristics, and the VSP ultimate electrochemical workstation (BioLogic Science Instruments, France) for CV and PEIS profiles.

Acknowledgements

This work is supported by the Startup Foundation of China Academy of Engineering Physics, Institute of Chemical Materials (KJCX201301 and KJCX201306) and NSFC (51403193). And W. N. acknowledges Ms. Changyan Guo for XRD characterization and Mr. Zemin Zhang for Raman characterization.

Notes and references

[a] Institute of Chemical Materials, China Academy of Engineering Physics (CAEP), Mianyang 621900, China. E-mail: edward.bwang@gmail.com, binwang@caep.cn; Fax: +86 816-2544426

[b] College of Polymer Science and Engineering, State Key Laboratory of Polymer Materials Engineering, Sichuan University, Chengdu 610065, China

[c] Sichuan Research Center of New Materials, Mianyang 621000, China

† Electronic Supplementary Information (ESI) available: Other miscellaneous complementary characterizations and illustrations. See DOI: 10.1039/c000000x/

1. A. S. Aricò, P. Bruce, B. Scrosati, J.-M. Tarascon and W. van Schalkwijk, *Nat. Mater.*, 2005, **4**, 366-377.
2. N.-S. Choi, Z. Chen, S. A. Freunberger, X. Ji, Y.-K. Sun, K. Amine, G. Yushin, L. F. Nazar, J. Cho and P. G. Bruce, *Angew. Chem. Int. Ed.*, 2012, **51**, 9994-10024.
3. Y. Gogotsi, *ACS nano*, 2014, **8**, 5369-5371.
4. F. Cheng, J. Liang, Z. Tao and J. Chen, *Adv. Mater.*, 2011, **23**, 1695-1715.
5. X. Chen, C. Li, M. Graetzel, R. Kostecki and S. S. Mao, *Chem. Soc. Rev.*, 2012, **41**, 7909-7937.
6. L. Zhang and M. Fang, *Nano Today*, 2010, **5**, 128-142.
7. J. Lee, S. Mahendra and P. J. Alvarez, *ACS nano*, 2010, **4**, 3580-3590.
8. W. Ni, B. Wang, J. Cheng, X. Li, Q. Guan, G. Gu and L. Huang, *Nanoscale*, 2014, **6**, 2618-2623.
9. F.-F. Cao, Y.-G. Guo and L.-J. Wan, *Energy Environ. Sci.*, 2011, **4**, 1634-1642.
10. A. L. M. Reddy, M. M. Shaijumon, S. R. Gowda and P. M. Ajayan, *Nano Lett.*, 2009, **9**, 1002-1006.
11. D.-J. Xue, S. Xin, Y. Yan, K.-C. Jiang, Y.-X. Yin, Y.-G. Guo and L.-J. Wan, *J. Am. Chem. Soc.*, 2012, **134**, 2512-2515.
12. Z. Sun, K. Xie, Z. A. Li, I. Sinev, P. Ebbinghaus, A. Erbe, M. Farle, W. Schuhmann, M. Muhler and E. Ventosa, *Chem. Eur. J.*, **20**, 2022-2030.
13. S. Xin, Y.-G. Guo and L.-J. Wan, *Acc. Chem. Res.*, 2012, **45**, 1759-1769.
14. S. Chabi, C. Peng, D. Hu and Y. Zhu, *Adv. Mater.*, 2014, **26**, 2440-2445.
15. B. Wang, J. Cheng, Y. Wu, D. Wang and D. He, *J. Mater. Chem. A*, 2013, **1**, 1368-1373.
16. J. Cheng, H. Xin, H. Zheng and B. Wang, *J. Power Sources*, 2013, **232**, 152-158.
17. W.-M. Zhang, J.-S. Hu, Y.-G. Guo, S.-F. Zheng, L.-S. Zhong, W.-G. Song and L.-J. Wan, *Adv. Mater.*, 2008, **20**, 1160-1165.
18. A. R. Kamali and D. J. Fray, *Rev. Adv. Mater. Sci*, 2011, **27**, 14-24.
19. L. Beaulieu, K. Eberman, R. Turner, L. Krause and J. Dahn, *Electrochem. Solid-State Lett.*, 2001, **4**, A137-A140.
20. J. Liu, S. Z. Qiao, J. S. Chen, X. W. D. Lou, X. Xing and G. Q. M. Lu, *Chem. Commun.*, 2011, **47**, 12578-12591.
21. R. Ghosh Chaudhuri and S. Paria, *Chem. Rev.*, 2011, **112**, 2373-2433.
22. K. T. Lee, Y. S. Jung and S. M. Oh, *J. Am. Chem. Soc.*, 2003, **125**, 5652-5653.
23. D. Deng and J. Y. Lee, *Chem. Mater.*, 2008, **20**, 1841-1846.
24. D. Deng, M. G. Kim, J. Y. Lee and J. Cho, *Energy Environ. Sci.*, 2009, **2**, 818-837.
25. N. Liu, H. Wu, M. T. McDowell, Y. Yao, C. Wang and Y. Cui, *Nano Lett.*, 2012.
26. Z. W. Seh, W. Li, J. J. Cha, G. Zheng, Y. Yang, M. T. McDowell, P.-C.

Hsu and Y. Cui, *Nat. commun.*, 2013, **4**, 1331.
27. X. W. Lou, C. M. Li and L. A. Archer, *Adv. Mater.*, 2009, **21**, 2536-2539.
28. X. W. Lou, J. S. Chen, P. Chen and L. A. Archer, *Chem. Mater.*, 2009, **21**, 2868-2874.
29. F. Zhang, C. Yuan, J. Zhu, J. Wang, X. Zhang and X. W. D. Lou, *Adv. Funct. Mater.*, 2013, **23**, 3909-3915.
30. W. Ni, Y. Wang and R. Xu, *Part. Part. Syst. Charact.*, 2013, **30**, 873-880.
31. P. Wu, N. Du, H. Zhang, C. Zhai and D. Yang, *ACS Appl. Mater. Interfaces*, 2011, **3**, 1946-1952.
32. D. Kim, D. Lee, J. Kim and J. Moon, *ACS Appl. Mater. Interfaces*, 2012, **4**, 5408-5415.
33. F. Nobili, I. Meschini, M. Mancini, R. Tossici, R. Marassi and F. Croce, *Electrochim. Acta*, 2013, **107**, 85-92.
34. I. Meschini, F. Nobili, M. Mancini, R. Marassi, R. Tossici, A. Savoini, M. L. Focarete and F. Croce, *J. power sources*, 2013, **226**, 241-248.
35. H. Wang, P. Gao, S. Lu, H. Liu, G. Yang, J. Pinto and X. Jiang, *Electrochim. Acta*, 2011, **58**, 44-51.
36. Y. Yu, L. Gu, C. Zhu, P. A. van Aken and J. Maier, *J. Am. Chem. Soc.*, 2009, **131**, 15984-15985.
37. Y. Yu, L. Gu, C. Wang, A. Dhanabalan, P. A. van Aken and J. Maier, *Angew. Chem. Int. Ed.*, 2009, **48**, 6485-6489.
38. J. Ye, H. Zhang, R. Yang, X. Li and L. Qi, *Small*, 2010, **6**, 296-306.
39. B. Cheng, J. M. Russell, Shi, L. Zhang and E. T. Samulski, *J. Am. Chem. Soc.*, 2004, **126**, 5972-5973.
40. D. Chen and L. Gao, *Chem. Phys. Lett.*, 2004, **398**, 201-206.
41. X. W. Lou, Y. Wang, C. Yuan, J. Y. Lee and L. A. Archer, *Adv. Mater.*, 2006, **18**, 2325-2329.
42. S. Ding, J. S. Chen, G. Qi, X. Duan, Z. Wang, E. P. Giannelis, L. A. Archer and X. W. Lou, *J. Am. Chem. Soc.*, 2010, **133**, 21-23.
43. S. Liang, X. Zhu, P. Lian, W. Yang and H. Wang, *J. Solid State Chem.*, 2011, **184**, 1400-1404.
44. B. Luo, B. Wang, X. Li, Y. Jia, M. Liang and L. Zhi, *Adv. Mater.*, 2012, **24**, 3538-3543.
45. D. Deng and J. Y. Lee, *Angew. Chem. Int. Ed.*, 2009, **48**, 1660-1663.
46. F. Han, Y. Bai, R. Liu, B. Yao, Y. Qi, N. Lun and J. Zhang, *Adv. Energy Mater.*, 2011, **1**, 798-801.
47. S. Yang, X. Feng, L. Zhi, Q. Cao, J. Maier and K. Müllen, *Adv. Mater.*, 2010, **22**, 838-842.
48. F. Croce, G. B. Appetecchi, L. Persi and B. Scrosati, *Nature*, 1998, **394**, 456-458.
49. M. Armand and J. M. Tarascon, *Nature*, 2008, **451**, 652-657.
50. W. H. Meyer, *Adv. Mater.*, 1998, **10**, 439-448.
51. J. W. Fergus, *J. power sources*, 2010, **195**, 4554-4569.
52. F. Boudin, X. Andrieu, C. Jehoulet and I. Olsen, *J.power sources*, 1999, **81**, 804-807.
53. Z. Wen, S. Cui, H. Kim, S. Mao, K. Yu, G. Lu, H. Pu, O. Mao and J. Chen, *J. Mater. Chem.*, 2012, **22**, 3300-3306.
54. S.-D. Seo, G.-H. Lee, A.-H. Lim, K.-M. Min, J.-C. Kim, H.-W. Shim, K.-S. Park and D.-W. Kim, *RSC Adv.*, 2012, **2**, 3315-3320.
55. M. Noh, Y. Kwon, H. Lee, J. Cho, Y. Kim and M. G. Kim, *Chem. Mater.*, 2005, **17**, 1926-1929.
56. X. Zhao, Z. Xia and D. Xia, *Electrochimica Acta*, 2010, **55**, 6004-6009.
57. I. Courtney, J. Tse, O. Mao, J. Hafner and J. Dahn, *Physical Review B*, 1998, **58**, 15583.
58. F. Nobili, M. Mancini, S. Dsoke, R. Tossici and R. Marassi, *J. power sources*, 2010, **195**, 7090-7097.
59. S. Nam, S. Kim, S. Wi, H. Choi, S. Byun, S.-M. Choi, S.-I. Yoo, K. T. Lee and B. Park, *J. Power Sources*, 2012, **211**, 154-160.
60. S. Luo, K. Wang, J. Wang, K. Jiang, Q. Li and S. Fan, *Adv. Mater.*, 2012, **24**, 2294-2298.
61. Y. S. Jung, A. S. Cavanagh, A. C. Dillon, M. D. Groner, S. M. George and S.-H. Lee, *J. Electrochem. Soc.*, 2010, **157**, A75-A81.
62. X. Fan, J. Shao, X. Xiao, X. Wang, S. Li, H. Ge and L. Chen, *Nano Energy*, 2014.
63. B. Luo, B. Wang, X. Li, Y. Jia, M. Liang and L. Zhi, *Adv. Mater.*, 2012, **24**, 3538-3543.
64. A. Todd, P. Ferguson, M. Fleischauer and J. Dahn, *Int. J. Energy Res.*, **34**, 535-555.
65. V. Aravindan, J. Sundaramurthy, E. N. Kumar, P. S. Kumar, W. C. Ling, R. von Hagen, S. Mathur, S. Ramakrishna and S. Madhavi, *Electrochim. Acta*, 2014, **121**, 109-115.
66. J. Hassoun, G. Derrien, S. Panero and B. Scrosati, *Adv. Mater.*, 2008, **20**, 3169-3175.

Journal Name RSCPublishing

COMMUNICATION

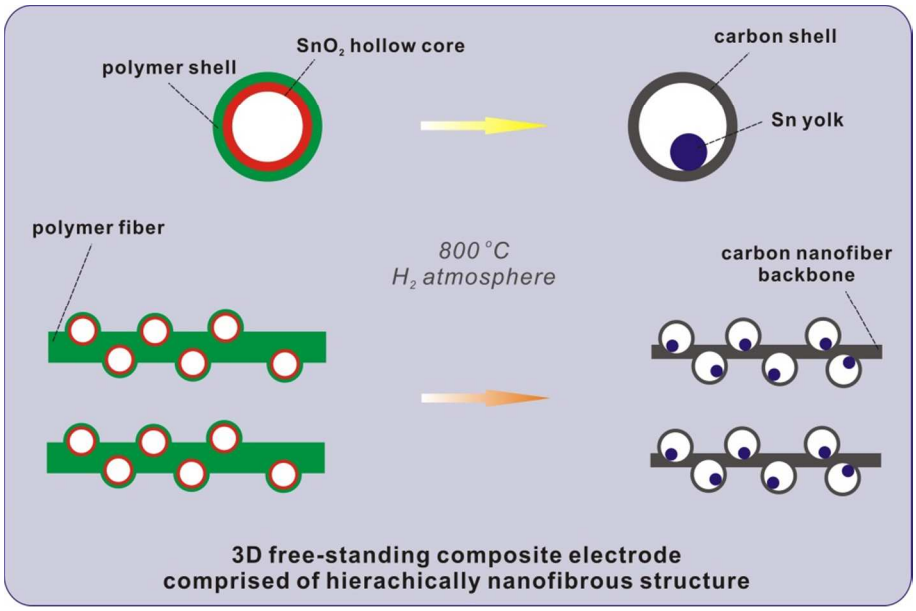

Scheme 1 Schematic illustration of the *in situ* reduction strategy for 3D composite electrode of yolk-shell Sn/C nanostructures integrated into nanofibrous backbones. The SnO_2 hollow spheres were embedded in electrospun polymer fibers, followed by the transformation into a Sn@C yolk-shell structure integrated in 3D nanofiber conductive networks as free-standing electrode materials.

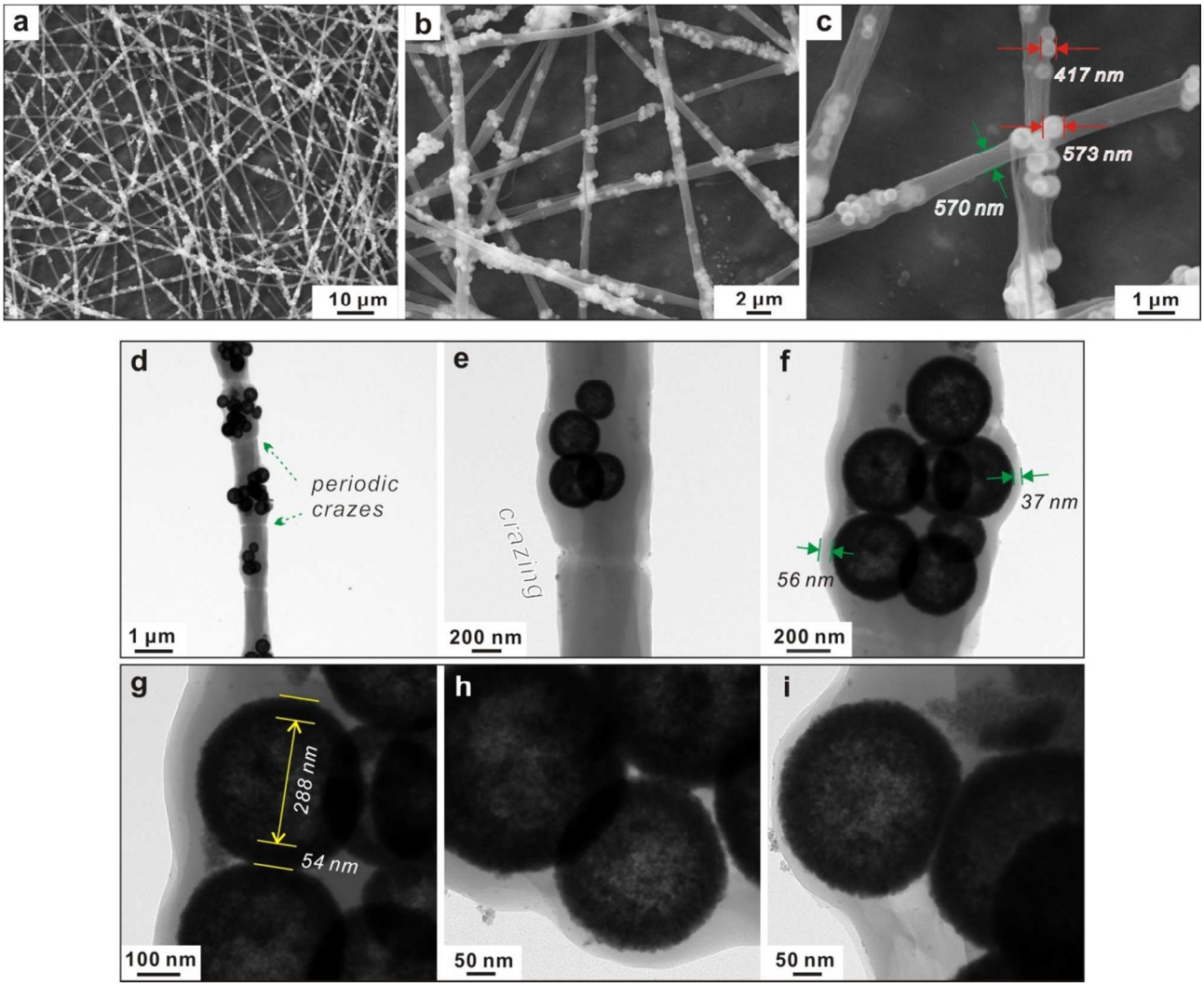

Fig. 1 (a–c) FESEM images of the hollow SnO_2/PAN core-shell free-standing film, of which PAN sub-micrometer fibers main diameter: ~600 nm, and the SnO_2@PAN core-shell subsystem structure main diameter: 400–550 nm. (d–i) TEM images of the as-prepared SnO_2@PAN composite fibers. The PAN coating layers show a main thickness of 30–70 nm (some thinner parts may be reduced to less than 10 nm), and the shell (~50 nm) of SnO_2 hollow spheres with hollow cavity size in the range of 150–300 nm, as the subsystem structure, was made of nanoparticles of 5–10 nm.

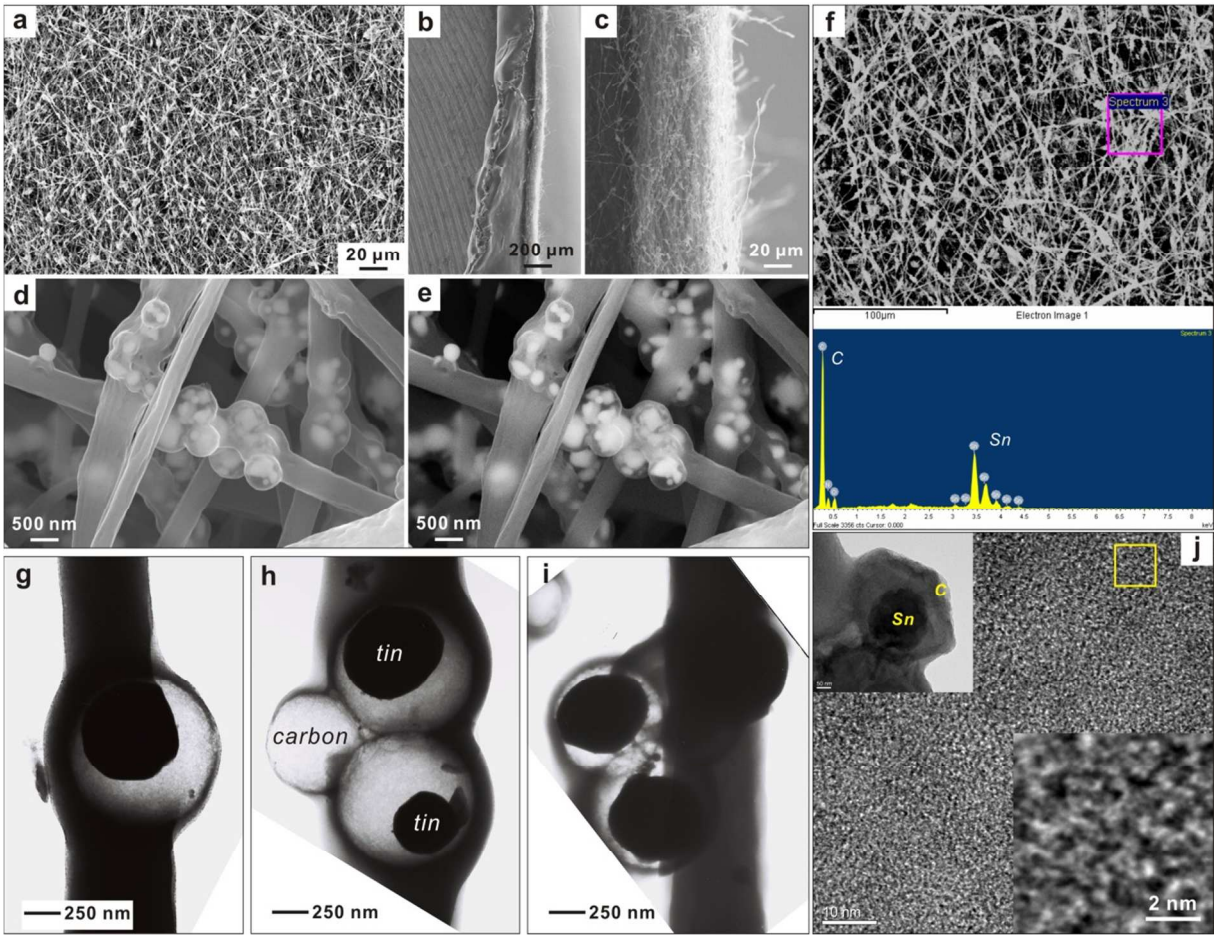

Fig. 2 (a–d) SEM images of the Sn/C yolk-shell free-standing film with thickness of ~40 μm. (e) SEM image of *d* by a backscattered electron imaging model. (f) EDS of the Sn@C yolk-shell flexible framework, which is sticked to an electrical conductive carbon tape and sputtering-coated with Au for 15 s. (g–j) TEM images of the abovementioned Sn@C yolk-shell structure, and the lower right inset of *j* shows a nanoporous/nanochannel structure of the carbon shell with some aligned small scale graphene layers. The large-scale SEM images of Sn@C nanocomposite and the cellular carbon shells after evaporation of Sn see Figure S1 and S2 in ESI†.

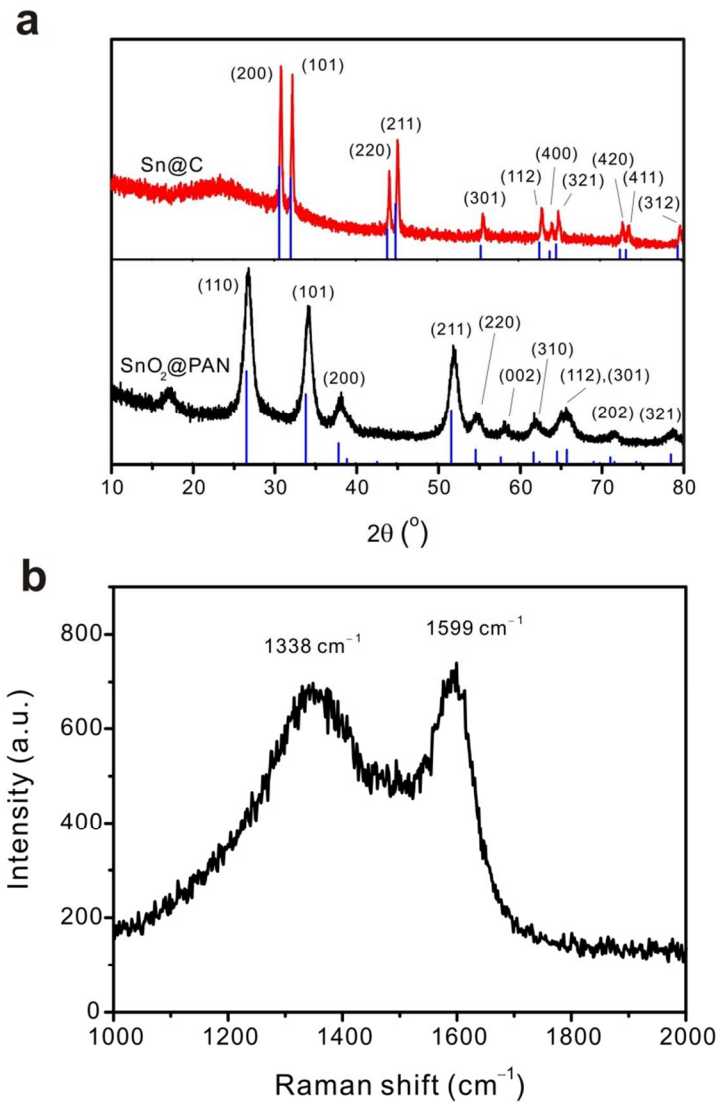

Fig. 3 (a) XRD patterns of the SnO_2/PAN core-shell and Sn/C yolk-shell free-standing composite film. JCPDS card no.: SnO_2 (cassiterite, #41-1445) and Sn (#86-2265). (b) Raman spectra of the as-prepared Sn/C composite film.

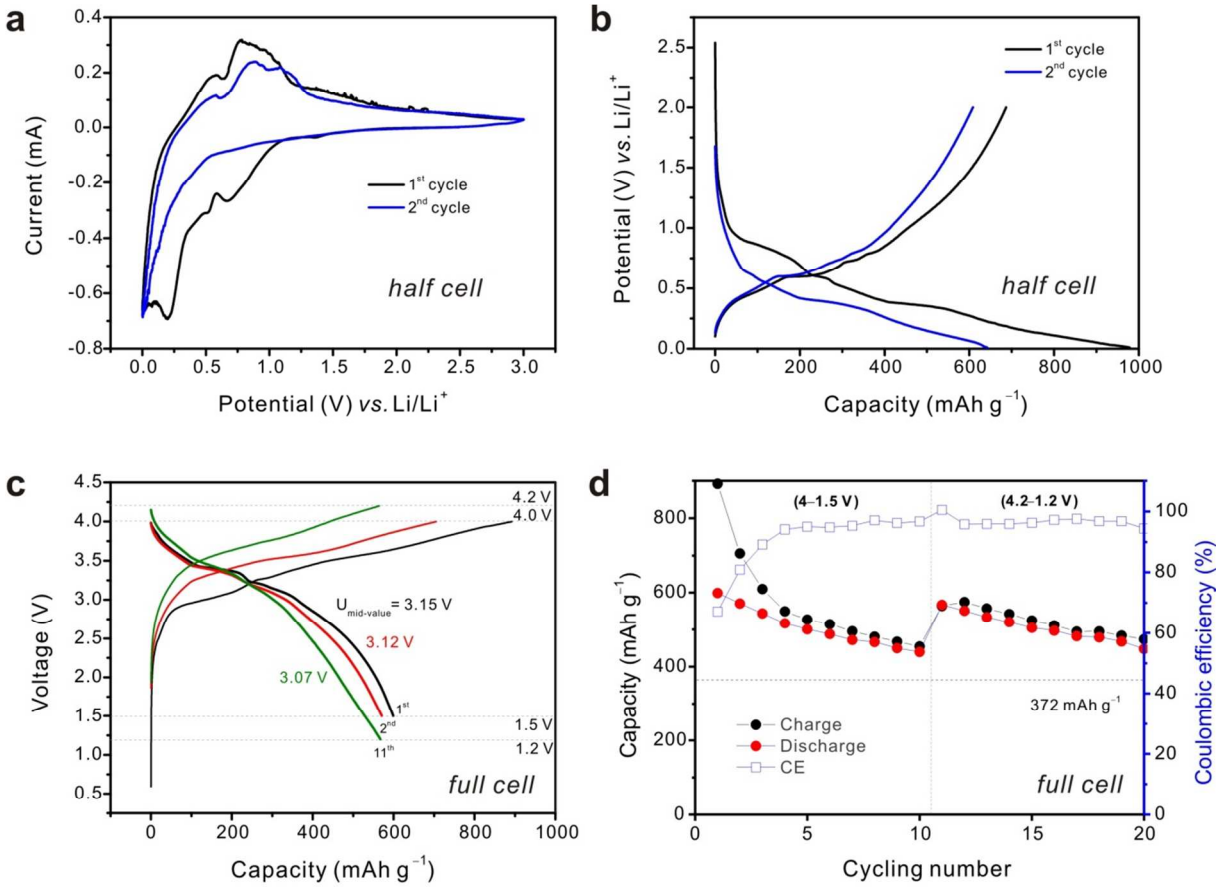

Fig. 4 (a) Cyclic voltammogram of the Sn/C free-standing nanocomposite film by pyrolysis in hydrogen, with a scanning rate of 0.05 mV s^{-1} over the potential range of 3–0 V *vs.* Li/Li^+. (b) Galvanostatic voltage–specific capacity profiles of the Sn/C composite film. (c) The full cell performance of the Sn@C nanocomposite as free-standing anode and commercial $LiCoO_2$ as cathode materials, with a mass ratio of 1:6.3 (Sn@C nanocomposite to $LiCoO_2$). (d) The cycling profile of the abovementioned full cell with varied charge and discharge cut-off potential windows. The capacities abovementioned are based on the Sn/C composite with Sn mass fraction of *ca.* 44%.

Graphical Abstract

Integrating complex Sn/C hollow elastic nanostructure into flexible nanofibers as ideal 3D composite electrodes were preliminarily developed and may have potential applications such as wearable energy devices.